



Inversion reflectance by apple tree canopy ground and unmanned aerial vehicle integrated remote sensing data

Ruiyang Yu¹ · Xicun Zhu^{1,2} · Xueyuan Bai¹ · Zhongyu Tian¹ · Yuanmao Jiang³ · Guijun Yang⁴

Received: 6 July 2020 / Accepted: 24 December 2020 / Published online: 15 February 2021
© The Botanical Society of Japan 2021

Abstract

To obtain accurate spatially continuous reflectance from Unmanned Aerial Vehicle (UAV) remote sensing, UAV data needs to be integrated with the data on the ground. Here, we tested accuracy of two methods to inverse reflectance, Ground-UAV-Linear Spectral Mixture Model (G-UAV-LSMM) and Minimum Noise Fraction-Pixel Purity Index-Linear Spectral Mixture Model (MNF-PPI-LSMM). At wavelengths of 550, 660, 735 and 790 nm, which were obtained by UAV multispectral observations, we calculated the canopy abundance based on the two methods to acquire the inversion reflectance. The correlation of the inversion and measured reflectance values was stronger in G-UAV-LSMM than MNF-PPI-LSMM. We conclude that G-UAV-LSMM is the better model to obtain the canopy inversion reflectance.

Keywords Apple tree canopy · Integrated · Inversion · Reflectance · Remote sensing

Introduction

The basis of quantitative remote sensing is acquiring accurate reflectance (Jin et al. 1986). Although reflectance measured by ground hyperspectrometer has higher precision (Du et al. 2011; Lee et al. 2004; Maire et al. 2004; Wei et al. 2017), it is only discrete single point data. We need accurate reflectance for spatially continuous regions. Unmanned Aerial Vehicle (UAV) remote sensing is widely used in agricultural quantitative remote sensing monitoring for spatially continuous regions. Because it is important to

acquire accurate reflectance for UAV remote sensing, the UAV sensor reflectance accuracy needs improvement.

Decomposition of mixed pixels is a vital method for improving the accuracy of reflectance. Endmember is an important component of spectral mixture model. At present, endmember extraction algorithms mainly include minimum noise fraction method, pure pixel index method, principal component transformation method, field measurement method, model simulation method and so on (Adams et al. 1995; De Asis and Omasa 2007; Dennison and Roberts 2003; Hu et al. 2004; Townshend et al. 2000; Zhu 2005). Many studies applied Multiple Endmember Spectral Mixture Analysis (MESMA) on remote sensing images, and allowed a linear combination of endmembers to vary in number and type on each pixel to explore the optimal endmember combination (Degerickx et al. 2019; Dennison and Roberts 2003; Fan 2015; Fernández-Manso et al. 2012; Quintano et al. 2013; Thorp et al. 2013). Some researchers (Cai 2010; Gu et al. 2007) extracted endmember spectrum of remote sensing images by Minimum Noise Fraction-Pure Pixel Index (MNF-PPI) method. Shanmugam et al. (2006) used endmember extraction algorithm to obtain endmember spectral characteristics of three kinds of ground objects after classification of ground objects from Indian remote sensing satellite IRS image and Landsat 5 TM image, including

✉ Xicun Zhu
zxc@sdau.edu.cn

¹ College of Resources and Environment, Shandong Agricultural University, Tai'an 271018, China

² National Engineering Laboratory for Efficient Utilization of Soil and Fertilizer Resources, College of Resources and Environment, Shandong Agricultural University, Tai'an 271018, China

³ College of Horticulture Science and Engineering, National Apple Engineering and Technology Research Center, Shandong Agricultural University, Tai'an 271018, China

⁴ National Engineering Research Center for Information Technology in Agriculture, Beijing 100097, China

vegetation, soil and water. Bian et al. (2014) derived each endmember from HJ satellite images by an adaptive selection endmember method.

Previous studies have extracted the spectral reflectance of the endmember from the satellite remote sensing images, or used the spectral mixture models to integrate the ground and satellite remote sensing data (Wang et al. 2012, 2013). However, the ground measured data was not used to integrate the UAV remote sensing data for reflectance inversion.

We chose the apple orchard as the research district, as apple cultivation is widespread in China (An et al. 2019; Fang et al. 2019; Han et al. 2019). We explored a better method for improving the inversion accuracy of apple tree canopy reflectance by comparing Minimum Noise Fraction-Pure Pixel Index-Linear Spectral Mixture Model (MNF-PPI-LSMM) and Ground-Unmanned Aerial Vehicle-Linear Spectral Mixture Model (G-UAV-LSMM), which were the two representative methods of mixed pixel decomposition with G-UAV integrated remote sensing data and only UAV remote sensing data.

Materials and methods

Study area

The study was executed outdoors in an apple orchard in Yedian town, Mengyin county, Linyi city, Shandong Province (Fig. 1) in eastern China on 10th, June 2019. Mengyin county is located in the central and southern of Shandong. The geographical scope is 117°45′—118°15′ E, 35°27′—36°02′ N, belonging to a temperate continental monsoon climate.

Experimental design

The data sources of the research were ground hyperspectral data and UAV multispectral data. The acquiring processing for the data is the following.

(1) Radiometric calibration was performed on the calibration board (whose reflectance is 1) of Sequoia sensor before flying. Low-altitude UAV was used for aerial photography, and four control points were set at four corners of the sampling area.

(2) 15 sample squares of 5 m × 5 m were arranged in the sampling area (50 m × 50 m) randomly. We located the coordinates of the center points of the sample squares. The multispectral images were taken with mosaic and radiometric calibration. Then the image was geometrically corrected using GPS coordinates of the four control points. The 15 sample squares were located on the UAV image to obtain multispectral reflectance.

(3) For each sample square, the apple tree canopy near the center point was selected to collect the canopy spectrum on the ground. The four spectrums of bare soil on the ground were measured at the north, south, west and east of the apple tree canopy. The average reflectance of 15 apple tree canopy samples and the 60 bare soil samples were taken as the endmember of apple tree canopy and bare soil. The reflectance of 15 apple tree canopy samples were used to validate the inversion reflectance.

UAV remote sensing data acquisition and preprocessing

We used the Dajiang Matrice 600 Pro UAV to carry the sensor, and a Parrot Sequoia Multispectral Camera, for aerial photography. There were four multispectral bands, including green band (GRE: 530–570 nm), red band (RED: 640–680 nm), red edge band (REG: 730–740 nm) and near-infrared band (NIR: 770–810 nm). The four center wavelengths of the bands were 550, 660, 735 and 790 nm. The flying altitude was 50 m. The multispectral remote sensing image was of the coordinates of WGS-84. The ground spatial resolution of the multispectral image was 5 cm. A total of 292 multispectral images of the aerial photography area were obtained. Pix4D software was used to take mosaic

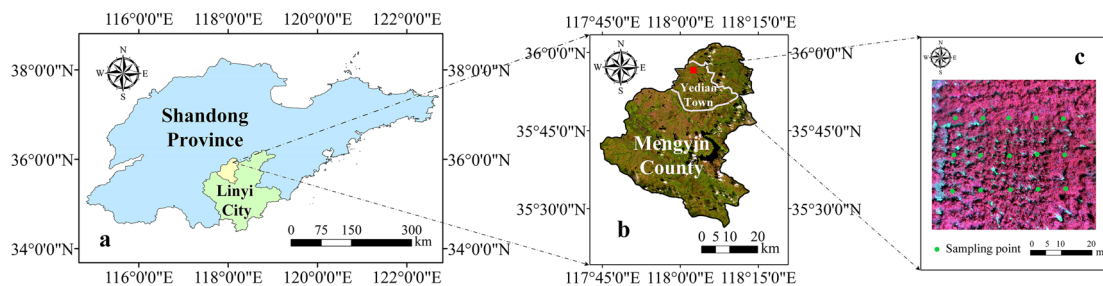


Fig. 1 Location of the study area. **a** Location of Linyi City in Shandong Province. **b** Location of study area in Yedian Town, Mengyin County. **c** Image of study area acquired by UAV. The green dots represent the sampling points

and radiate the multispectral images to obtain multispectral images with surface mixed reflectance data.

Acquisition of ground hyperspectral data

During UAV aerial photography, the spectral collection of apple tree canopy was conducted by FieldSpec4 (ASD Inc., USA). The spectral range of FieldSpec 4 is 350–2500 nm. Between 350 and 1000 nm, the spectral sampling interval is 1.4 nm and the spectral resolution is 3 nm. Between 1000 and 2500 nm, the sampling interval is 2 nm and spectral resolution is 8 nm.

The determination time was 10:00–12:00. The weather was clear and cloudless. We optimized the reflectance of the UAV images with a standard whiteboard (a reference with the reflectance of 1). During the canopy spectral measurement, the measuring probe was aligned downward vertically, so that the probe center was above the canopy directly, where the vertical height was 1.5 m from the top of canopy. According to the appropriate adjustment of canopy size, the field of view was 25°. We carried out the spectral data acquisition 5 times at each canopy sample (5 m × 5 m) with its average as reflectance of the canopy sample. When determining the spectrum of bare soil, we ensured that the probe center was directly above the target at 1.5 m. According to the target size, the field of view was also 25°. We collected five times at each bare soil sample for spectral data, with its average as the reflectance of the bare soil sample.

Mixed pixel decomposition method

Mixed pixel decomposition is the process where we research the composition and proportion of mixed pixels by remote sensing images, including endmember extraction and abundance inversion. Endmember extraction refers to determining the basic features that make up the mixed pixel, and abundance inversion refers to calculating the proportion of each basic feature in the mixed pixel (De Asis and Omasa 2007). The inversion reflectance can be defined as the product of the spectral reflectance of different endmember components and their abundance (Wang et al. 2012). G-UAV-LSMM took the measured hyperspectral data of canopy and bare soil as the endmember, and then we used LSMM for abundance inversion to obtain the G-UAV-LSMM canopy inversion reflectance. MNF-PPI-LSMM can distinguish canopy and bare soil by visual interpretation. The endmember reflectance of the canopy and bare soil, whose PPI values are the maximum value, can be extracted by MNF-PPI method, respectively. Then, we used the LSMM for abundance inversion to obtain MNF-PPI-LSMM canopy inversion reflectance.

G-UAV-LSMM

To unify the hyperspectral data obtained by the ground spectrometer with the multi-spectral image data of the low-altitude UAV, we selected the measured hyperspectral data at wavelengths of 550, 660, 735 and 790 nm. We took the linear mixed pixel decomposition for the average surface mixed reflectance (ρ_a) of each band at every sample square by the measured canopy and bare soil endmember reflectance at these wavelengths. G-UAV-LSMM canopy inversion reflectance (ρ_b) was obtained with the multiple of the abundance and the canopy endmember spectrum. The formula of LSMM (Liu and Yao 2009) is:

$$r_i = \sum_{j=1}^m \alpha_{ij} e_j + \varepsilon_j \quad (1)$$

In formula (1), r_i is the surface mixed reflectance. α_{ij} is the weight of e_j in r_i , which is called abundance. e_j is the endmember spectral reflectance. ε_j is the error term, which reflects the random noise of the data. The physical meaning of α_{ij} is the area ratio of the j^{th} endmember in the i^{th} pixel. m is the total number of endmembers. Therefore, the constraint conditions should be followed, as shown in formula (2–3):

$$\alpha_{ij} \geq 0, \forall i, j \quad (2)$$

$$\sum_{j=1}^m \alpha_{ij} = 1, i = 1, 2, \dots, n \quad (3)$$

MNF-PPI-LSMM

Each wavelength of UAV multispectral remote sensing image was taken with the MNF-PPI processing, and the canopy and bare soil endmember spectral reflectance was obtained. We took the linear mixed pixel decomposition for the surface mixed reflectance of each band at every sample square using these canopy and bare soil spectral reflectance, then we got the canopy abundance value of every sample square. The canopy abundance value multiplied by canopy endmember spectral reflectance of each sample square was MNF-PPI-LSMM canopy inversion reflectance (ρ_c).

The researchers (Green et al. 1988; Lee et al. 1990) took MNF conversion and then modified it. The high-pass filter template is used to filter the whole image data block with the same quality, and the noise covariance matrix C_N is obtained, which is diagonally transformed into the matrix D_N .

$$D_N = U^T C_N U \quad (4)$$

In formula (4), D_N is the diagonal matrix whose eigenvalues of C_N are arranged in descending order. U is an orthogonal matrix of eigenvectors.

$$I = P^T C_N P \quad (5)$$

$$P = U D_N^{-1/2} \quad (6)$$

In formula (5–6), I is the identity matrix. P is the transformation matrix. When P is applied to the image X , the original image is projected into the new space through $Y = PX$ transformation. The noise has unit variance and is not correlated among the bands in the generated transformation data. Standard principal component transformation is performed on noise data.

$$C_{D-adj} = P^T C_D P \quad (7)$$

In formula (7), C_D is the covariance matrix of image. C_{D-adj} is the matrix after P transformation, which is further diagonalized to the matrix D_{D-adj} .

$$D_{D-adj} = V^T C_{D-adj} V \quad (8)$$

In formula (8), D_{D-adj} is the diagonal matrix whose eigenvalues are arranged in descending order by C_{D-adj} . V is an orthogonal matrix of eigenvectors. Through the above two steps, the transformation matrix T_{MNF} is obtained, $T_{MNF} = PV$.

The reflectance of apple tree canopy and bare soil pixel with the highest PPI values in various quadrates was used to represent the reflectance of canopy and bare soil endmember through MNF processing. Then the LSMM was used to inverse the abundance. The formula and constraint conditions of LSMM are the same as formulas (1–3).

Inversion accuracy evaluation

The determination coefficient (R^2), Root Mean Square Error ($RMSE$) and Residual Prediction Deviation (RPD) are used to evaluate the reflectance accuracy of canopy inversion. R^2 is the measure of the degree of correlation between variables, which determines the degree of correlation. The larger R^2 is, the closer the predicted value is to the measured value. $RMSE$ is used to measure the deviation between the predicted value and the measured value. The less the $RMSE$ is, the better the prediction effect is. RPD is an effective indicator to judge the prediction effect of the model. SD is standard deviation. When $RPD > 2$, it indicates that the model has a good effect and can be used for quantitative analysis. When $1.8 < RPD < 2.0$, it indicates that the model is effective and can be used for quantitative estimation. When $1.4 < RPD < 1.8$, it indicates that the model can roughly estimate the sample. When $RPD < 1.4$, the model

is less effective (Gaston et al. 2010). Formula (9–12) is the calculation formula of each indicator:

$$R^2 = \frac{\sum_{i=1}^N (y_i - \bar{y})(x_i - \bar{x})^2}{\sum_{i=1}^N (y_i - \bar{y})^2 \sum_{i=1}^N (x_i - \bar{x})^2} \quad (9)$$

$$RMSE = \sqrt{\frac{1}{N} \sum_{i=1}^N (y_i - x_i)^2} \quad (10)$$

$$RPD = \frac{SD}{RMSE} \quad (11)$$

$$SD = \sqrt{\frac{1}{N-1} \sum_{i=1}^N (x_i - \bar{x})^2} \quad (12)$$

In the formula (9–12), x is the measured canopy reflectance. \bar{x} is the average measured canopy reflectance. y is the inversion reflectance. \bar{y} is the average inversion reflectance. N is the amount of samples. i is the number of the samples.

Results

Figure 2 refers to the average ground hyperspectral and UAV multispectral curves of the 15 canopy samples, which reflect their spectral characteristics. As can be seen from Fig. 2, the

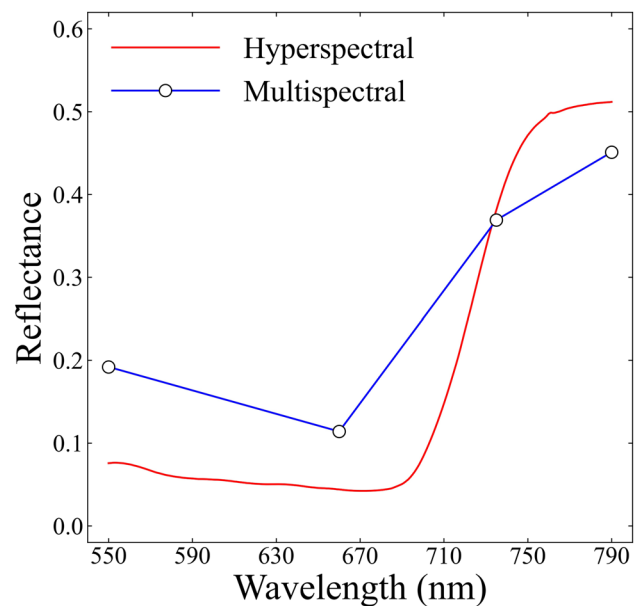


Fig. 2 Apple tree canopy average hyperspectral and multispectral curves

hyperspectral curve has an absorption valley at 690 nm, and the reflectance increases at 735 nm sharply, while it is relatively stable at 760–790 nm. The multispectral curve shows a trend of decline from 550 to 660 nm. The reflectance rises gradually from 660 to 735 nm. There is an obvious absorption valley at 660 nm because of the strong absorption to the red band. The curve presents an increasing tendency from 735 to 790 nm, owing to the strong reflection of the near infrared band. Through the comparison for the hyperspectral and multispectral curves, it is found that the hyperspectral curve can reflect the continuous spectral characteristics, and the multispectral curve is a line connected by discrete points.

Splicing and radiometric calibration of the multispectral image were both completed in Pix4D software. Then ρ_a was obtained directly, and we used ρ_a to inverse reflectance based on G-UAV-LSMM and MNF-PPI-LSMM. We obtained the measured canopy and bare soil endmember spectral reflectance by the ground spectrometer. They were selected at the central wavelengths of 550, 660, 735 and 790 nm. Figure 3a shows the canopy abundance of each pixel obtained by the G-UAV-LSMM method. The results show that the canopy abundance value is higher at the top of the tree canopy, while the canopy abundance value is lower at the edge of the tree canopy, which is caused by the greater influence of bare soil spectrum on the edge. The G-UAV-LSMM canopy inversion reflectance is the measured hyperspectral reflectance selected at the central wavelengths of the UAV multispectral data multiplied by the abundance α .

We used the MNF-PPI method to obtain the canopy and bare soil endmember spectral reflectance from the multispectral image. Figure 3b shows the canopy abundance values of each pixel obtained by MNF-PPI-LSMM method.

The results show that the canopy abundance value at the top of the canopy was higher, but the canopy abundance value at the edge of the canopy was lower, which was caused by the great influence of bare soil spectrum on the edge. It is consistent with the law of the canopy abundance value obtained by the G-UAV-LSMM method. The MNF-PPI-LSMM canopy inversion reflectance is canopy abundance α multiplied by e_j , of which PPI is the highest.

Figure 4a–d are 1:1 scatter plots between the measured and inversion reflectance values based on G-UAV-LSMM method at central wavelengths of 550, 660, 735 and 790 nm, respectively. The results show that the R^2 of fitting equation composed by measured reflectance (ρ) and ρ_b are 0.845, 0.869, 0.861 and 0.871. The $RMSE$ are 0.005, 0.007, 0.017 and 0.025. The RPD are 2.432, 1.891, 2.507 and 2.275 by the G-UAV-LSMM method, respectively.

Figure 5a–d are the 1:1 scatter plots of the measured and predicted canopy reflectance values based on MNF-PPI-LSMM method at the central wavelength of 550, 660, 735 and 790 nm respectively. The results show that the R^2 of fitting equation composed by ρ and ρ_c are 0.709, 0.728, 0.760 and 0.794. The $RMSE$ are 0.012, 0.010, 0.024 and 0.042. The RPD are 1.013, 1.324, 1.776 and 1.354 by the MNF-PPI-LSMM method. The comparison shows that G-UAV-LSMM can better inverse the canopy reflectance of apple trees.

Discussion

The surface mixed reflectance mentioned in this study was the reflectance of radiance values of multispectral image after radiometric calibration. Canopy inversion reflectance

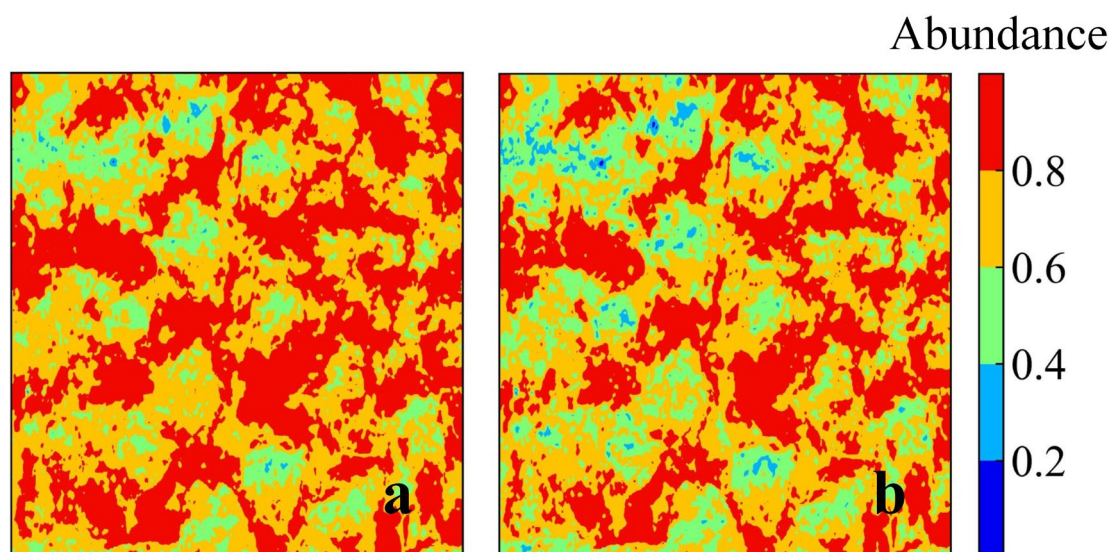
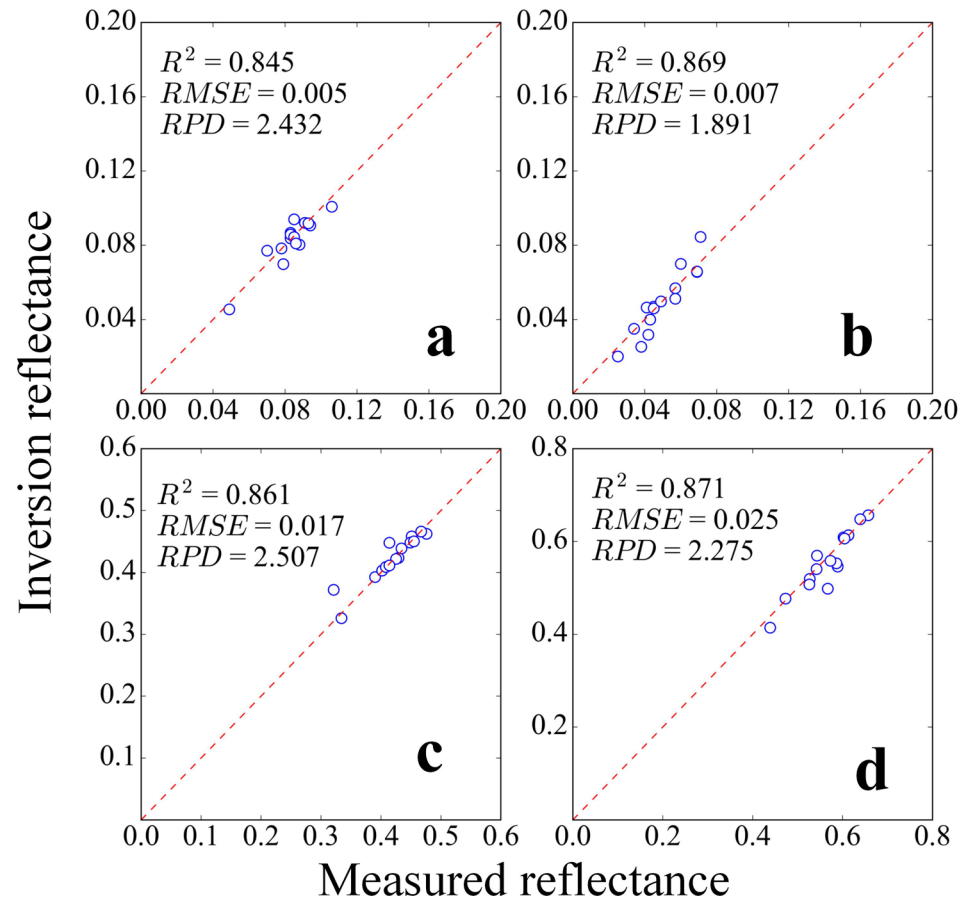


Fig. 3 Canopy abundance based on **a** G-UAV-LSMM and **b** MNF-PPI-LSMM

Fig. 4 1:1 scatter plots of measured and inversion reflectance based on G-UAV-LSMM at wavelengths of **a** 550 nm, **b** 660 nm, **c** 735 nm and **d** 790 nm



is the canopy reflectance obtained after mixed pixel decomposition (Wang et al. 2012, 2013), including the canopy inversion reflectivity obtained by MNF-PPI-LSMM and G-UAV-LSMM methods. In this study, the reflectance inversion methods were mixed pixel decomposition methods.

This research introduced the canopy reflectance inversion method, G-UAV-LSMM, which integrated the ground hyperspectral and UAV remote sensing data. Its accuracy was higher than that of MNF-PPI-LSMM, because it obtained the endmember spectrum through the ground hyperspectral data. The PPI algorithm used the spectral reflectance with maximum PPI as components. PPI algorithm accuracy depended on the endmember spectrum which was chosen (Zeng et al. 2009). The accuracy of PPI was affected by the phenomenon of the different spectrum in the same kind of item, which led to the lower accuracy of canopy inversion reflectance obtained by the MNF-PPI-LSMM method.

The accuracy of canopy inversion reflectance is affected by soil background (Liu et al. 2018). At the same time, the inversion of canopy reflectance taken by the G-UAV-LSMM method requires the support of the measured hyperspectral data on the ground. Because of the limitation of actual conditions, it is impossible to obtain the measured hyperspectral reflectance of all locations in the aerial photography area.

Therefore, the most representative sites in the aerial photography area, such as the four corners and center point, are selected to obtain the measured average hyperspectral reflectance data of the canopy and bare soil as the endmember spectral reflectance of all pixels of the study area. Every time we get UAV multispectral images, we should obtain the measured ground reflectance data of the canopy and bare soil as the endmember spectrum on the most representative sites of the aerial photography area. The aim is to make sure that the endmember spectrum can represent the canopy and bare soil spectrum for each aerial photography area.

Our study also had some shortcomings. It did not consider the influence of the spectral resolution of UAV multispectral and ground measured hyperspectral data on the G-UAV-LSMM model. It ignored the influence of cloud, which needs further research to be incorporated to the model. Also, we need to study how the difference in spectral resolution and the sky condition affect the inversion accuracy. With the improvement of the related technologies and parameters, the inversion accuracy will be improved. More accurate canopy reflectance data will be obtained by G-UAV remote sensing data.

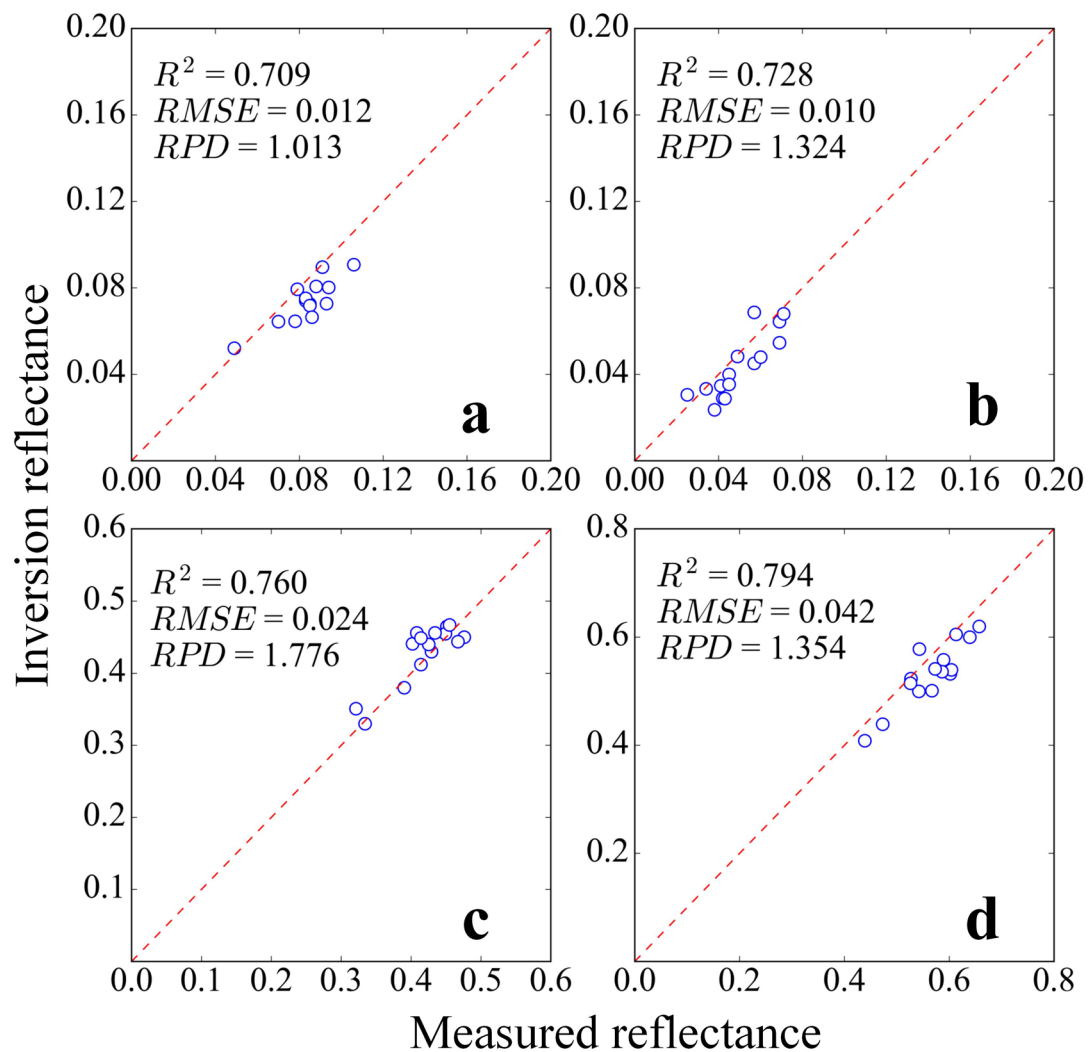


Fig. 5 1:1 scatter plots of measured and inversion reflectance based on MNF-PPI-LSMM at wavelengths of **a** 550 nm, **b** 660 nm, **c** 735 nm and **d** 790 nm

Conclusion

We explored the integrating method of ground and UAV remote sensing data to inverse the canopy reflectance. The accuracy of the canopy inversion reflectance obtained by G-UAV-LSMM was higher than that of MNF-PPI-LSMM at the central wavelengths of 550, 660, 735 and 790 nm. Therefore, G-UAV-LSMM had a better effect on the reflectance inversion for apple tree canopy.

Acknowledgements This research was supported by the National Key Research and Development Program of China, 2017YFE0122500; National Natural Science Foundation of China, 41671346; Funds of Shandong “Double Tops” Program, SYL2017XTTD02; Shandong major scientific and technological innovation project: Research demonstration and extension of orchard irrigation and fertilization in accurate management, 2018CXGC0209; The Taishan Scholar Assistance Program from Shandong Provincial Government.

Author contributions Conceptualization, R. Y. Y. and X. C. Z.; Data curation, R. Y. Y.; Investigation, R. Y. Y., X. C. Z., Z. Y. T. and X. Y. B.; Methodology, R. Y. Y.; Project administration, X. C. Z. and G. J. Y.; Resources, X. C. Z.; Software, R. Y. Y.; Supervision, Y. M. J. and G. J. Y.; Validation, X. C. Z., Z. Y. T. and X. Y. B.; Visualization, R. Y. Y.; Writing—original draft, R. Y. Y.; Writing—review and editing, R. Y. Y., X. C. Z. and Z. Y. T.

References

- Adams JB, Sabol DE, Kapos V et al (1995) Classification of multi-spectral images based on fractions of endmembers: application to land-cover change in the brazilian amazon. *Remote Sens Environ* 52:137–154. [https://doi.org/10.1016/0034-4257\(94\)00098-8](https://doi.org/10.1016/0034-4257(94)00098-8)
- An JP, Zhang XW, Bi SQ et al (2019) MdbHLH93, an apple activator regulating leaf senescence, is regulated by ABA and MdbT2 in antagonistic ways. *New Phytol* 222:735–751. <https://doi.org/10.1111/nph.15628>

- Bian JH, Li AN, Zhang ZJ et al (2017) Monitoring fractional green vegetation cover dynamics over a seasonally inundated alpine wetland using dense time series HJ-1A/B constellation images and an adaptive endmember selection LSMM model. *Remote Sens Environ* 197:98–114. <https://doi.org/10.1016/j.rse.2017.05.031>
- Cai W (2010) Recognition and area estimation of wheat based on mixed pixel decomposition of MODIS remote sensing data. Dissertation, Shandong Normal University
- De Asis AM, Omasa K (2007) Estimation of vegetation parameter for modeling soil erosion using linear spectral mixture analysis of landsat ETM data. *ISPRS J Photogramm* 62:309–324. <https://doi.org/10.1016/j.isprsjprs.2007.05.013>
- Degerickx J, Roberts DA, Somers B (2019) Enhancing the performance of multiple endmember spectral mixture analysis (MESMA) for urban land cover mapping using airborne lidar data and band selection. *Remote Sens Environ* 221:260–273. <https://doi.org/10.1016/j.rse.2018.11.026>
- Dennison PE, Roberts DA (2003) Endmember selection for multiple endmember spectral mixture analysis using endmember average RMSE. *Remote Sens Environ* 87:123–135. [https://doi.org/10.1016/S0034-4257\(03\)00135-4](https://doi.org/10.1016/S0034-4257(03)00135-4)
- Du HQ, Fan WL, Zhou GM et al (2011) Retrieval of canopy closure and lai of moso bamboo forest using spectral mixture analysis based on real scenario simulation. *IEEE T Geosci Remote* 49:4328–4340. <https://doi.org/10.1109/TGRS.2011.2107327>
- Fan FL, Deng YB (2015) Enhancing endmember selection in multiple endmember spectral mixture analysis (MESMA) for urban impervious surface area mapping using spectral angle and spectral distance parameters. *Int J Appl Earth Observ* 36:103–105. <https://doi.org/10.1016/j.jag.2014.11.004>
- Fang HC, Dong YH, Yue XX et al (2019) Mdc04 interaction mediates crosstalk between uv-b and high temperature to control fruit coloration in apple. *Plant Cell Physiol* 60:1055–1066. <https://doi.org/10.1093/pcp/pcz023>
- Fernández-Manso A, Quintano C, Roberts D (2012) Evaluation of potential of multiple endmember spectral mixture analysis (MESMA) for surface coal mining affected area mapping in different world forest ecosystems. *Remote Sens Environ* 127:181–193. <https://doi.org/10.1016/j.rse.2012.08.028>
- Gaston E, Frias JM, Cullen PJ et al (2010) Prediction of polyphenol oxidase activity using visible near-infrared hyperspectral imaging on mushroom (*Agaricus bisporus*) caps. *J Agr Food Chem* 58:6226–6233. <https://doi.org/10.1021/jf100501q>
- Green AA, Berman M, Switzer P et al (1988) A transformation for ordering multispectral data in terms of image quality with implications for noise removal. *IEEE T Geosci Remote* 26:65–74. <https://doi.org/10.1109/36.3001>
- Gu HY, Li HT, Yang JH (2007) The remote sensing image fusion method based on minimum noise fraction. *Remote Sens Land Res* 2:53–55
- Han PL, Dong YH, Gu KD et al (2019) The apple U-box E3 ubiquitin ligase MdPUB29 contributes to activate plant immune response to the fungal pathogen *Botryosphaeria dothidea*. *Planta* 249:1177–1188. <https://doi.org/10.1007/s00425-018-03069-z>
- Hu BX, Miller JR, Chen JM et al (2004) Retrieval of the canopy leaf area index in the boreas flux tower sites using linear spectral mixture analysis. *Remote Sens Environ* 89:176–188. <https://doi.org/10.1016/j.rse.2002.06.003>
- Jin LF, Lu SH, Zhu XH (1986) RS-II 4-Channel spectrometer and its specification. *J Remote Sens* 1:129–131
- Le Maire G, François C, Dufrêne E (2004) Towards universal broad leaf chlorophyll indices using PROSPECT simulated database and hyperspectral reflectance measurements. *Remote Sens Environ* 89:1–28. <https://doi.org/10.1016/j.rse.2003.09.004>
- Lee ZP, Carder KL (2004) Absorption spectrum of phytoplankton pigments derived from hyperspectral remote-sensing reflectance. *Remote Sens Environ* 89:361–368. <https://doi.org/10.1016/j.rse.2003.10.013>
- Lee JB, Woodyatt AS, Berman M (1990) Enhancement of high spectral resolution remote-sensing data by a noise-adjusted principal components transform. *IEEE T Geosci Remote* 28:295–304. <https://doi.org/10.1109/36.54356>
- Liu J, Yao GQ (2009) Research on the methods of unmixing the mixed pixels. *Computer Know Tech* 5:3499–3500
- Liu SS, Li LT, Gao WH et al (2018) Diagnosis of nitrogen status in winter oilseed rape (*Brassica napus* L.) using in-situ hyperspectral data and unmanned aerial vehicle (UAV) multispectral images. *Comput Electron Agr* 151:185–195. <https://doi.org/10.1016/j.compag.2018.05.026>
- Quintano C, Fernández-Manso A, Roberts DA (2013) Multiple end-member spectral mixture analysis (MESMA) to map burn severity levels from Landsat images in Mediterranean countries. *Remote Sens Environ* 136:76–88. <https://doi.org/10.1016/j.rse.2013.04.017>
- Shanmugam P, Ahn YH, Sanjeevi S (2006) A comparison of the classification of wetland characteristics by linear spectral mixture modelling and traditional hard classifiers on multispectral remotely sensed imagery in southern India. *Ecol Model* 194:379–394. <https://doi.org/10.1016/j.ecolmodel.2005.10.033>
- Thorp KR, French AN, Rango A (2013) Effect of image spatial and spectral characteristics on mapping semi-arid rangeland vegetation using multiple endmember spectral mixture analysis (MESMA). *Remote Sens Environ* 132:120–130. <https://doi.org/10.1016/j.rse.2013.01.008>
- Townshend JRG, Huang C, Kalluri SNV et al (2000) Beware of per-pixel characterization of land cover. *Int J Remote Sens* 21:839–843. <https://doi.org/10.1080/014311600210641>
- Wang L, Zhao GX, Zhu XC et al (2012) Quantitative remote sensing retrieval of apple tree canopy reflectance at blossom stage in hilly area. *Chin J Appl Ecol* 23:2233–2241
- Wang L, Zhao GX, Zhu XC et al (2013) Satellite remote sensing retrieval of canopy nitrogen nutritional status of apple trees at blossom stage. *Chin J Appl Ecol* 24:2863–2870
- Wei CW, Huang JF, Wang XZ et al (2017) Hyperspectral characterization of freezing injury and its biochemical impacts in oilseed rape leaves. *Remote Sens Environ* 195:56–66. <https://doi.org/10.1016/j.rse.2017.03.042>
- Zeng Y, Schaepman ME, Wu BF et al (2009) Quantitative forest canopy structure assessment using an inverted geometric-optical model and upscaling. *Int J Remote Sens* 30:1385–1406. <https://doi.org/10.1080/01431160802395276>
- Zhu HL (2005) Linear spectral unmixing assisted by probability guided and minimum residual exhaustive search for subpixel classification. *Int J Remote Sens* 26:5585–5601. <https://doi.org/10.1080/01431160500181408>

Publisher's Note Springer Nature remains neutral with regard to jurisdictional claims in published maps and institutional affiliations.